# Supplementary Information

## Bridging Particle-Scale Lithiation Mechanisms and Macroscopic Performance in High-Energy Density Si Anodes via Time-resolved Full 3D Visualisation

Michael Häusler [a], Rahulkumar J. Sinojiya [a], Olga Stamati [b], Julie Villanova [c], Christoph Stangl [d], Stefan Koller [d], Roland Brunner [a]*

**Author Affiliation**

[a] Materials Center Leoben Forschung GmbH, 8700 Leoben, Austria

[b] Univ. Grenoble Alpes, CNRS, Grenoble INP, 3SR, 38000 Grenoble, France

[c] ESRF- The European Synchrotron, ID16B, 38000 Grenoble, France

[d] Varta Innovation GmbH, 8020 Graz, Austria

* corresponding author. Email: roland.brunner@mcl.at

# Supplementary Note 1 - Material and Electrode Preparation

## Slurry Formulation & Casting

- **Anode Slurry Composition:**
  - 89 wt% micron-sized silicon particles (median size: 3–7 µm)
  - 9 wt% polyacrylic acid (PAA)-based binder
  - 1.8 wt% carbon black
  - 0.2 wt% single-walled carbon nanotubes (SWCNTs)
- **Mixing Protocol:** Weighed carbon black, SWCNTs and binder were dispersed in deionized water for 4 hours at 900 rpm, using an IKA EUROSTAR 20 dispersing unit. After addition of active material, the slurry was homogenized at [50 rpm] for [2 h] using a planetary mixer ([-HIVIS MIXTM]).
- **Coating & Drying:** Slurry was cast onto 10 µm-thick copper foil via doctor-blade technique, dried under vacuum at 80 °C for 12 h, and calendered to achieve a final thickness of [20 µm] (areal loading 3 mg $cm^{-2}$; theoretical areal capacity ~11 mAh $cm^{-2}$).

## Electrode Disk Fabrication

### Mechanical Punching (Preliminary Tests)

- A 1 mm-diameter hole punch tool was used to produce electrode disks. However, as shown in **Fig. S2a**, mechanical punching resulted in:
  - Edge tearing of the Si composite layer
  - Bending of the 10 µm copper current collector, leading to non-uniform circularity (~±0.05 mm)
  - Unwanted X-ray scattering from curled copper edges, compromising tomography imaging quality as shown in **Fig. S3**
- These defects significantly affected cell performance, as the edge area constitutes a relatively large portion of the total active area.

### Femtosecond Laser Micromachining

- **Instrument & General Settings:** 3D Micromac microPREP PRO (femtosecond laser) was used at 35 mW average power, repetitions [300], repetition rate [60 kHz], scan speed [300 mm/s]. The femtosecond laser system, equipped with an optimized optical setup, enables rapid material removal with nanometre-level precision.
- **Cutting Sequence Optimization:**
  1. **Copper-Side Milling (Suboptimal):** When milling from the copper side (**Fig. S2b**), significant copper redeposition occurred on the Si electrode sidewall, visible as bright rims in SEM/optical images - risking unwanted side reactions during lithiation.
  2. **Silicon-Side First Milling (Preferred):** Initiating cuts on the Si material side followed by Cu foil (**Fig. S2c**) yielded:
     - Clean, perfectly circular disks (d = 1.100 mm ± 0.001 mm)
     - Sharp, flat edges without redeposition artefacts
     - Mechanically robust disks suitable for electrochemical cycling and minimizing X-ray artefacts

# Supplementary Note 2 - In situ Cell Assembly

All assembly steps were executed in an Ar-filled glovebox to avoid moisture/oxygen contamination. Metadata files track every component, dimension, and environmental condition.

## Cell Housing & Sealing

- **Housing Material:** PFA tubing (ID = 1.6 mm, OD = 3.2 mm; low X-ray attenuation, chemical resistance).
- **End Mounts:** Stainless steel threaded mounts inserted into both ends. Interfaces sealed with acetone soluble lacquer to maintain air tightness of the cell.

## Electrode & Separator Stack

- **Electrodes:**
  - Anode disk (d = 1.100 mm, 11 mAh $cm^{-2}$)
  - Cathode disk (d = 1.100 mm, 3.5 mAh $cm^{-2}$)
- **Separator:** Non-woven polypropylene (d = 1.5 mm), soaked in 0.5 µL electrolyte (1 M $LiPF_6$ in FEC:DEC 2:8 v/v + 2 wt% VC).
- **Stack Pressure:** A spring-loaded contact inserted through the upper mount provided adjustable pressure (0.01–1.5 MPa). Pre-compressed to 0.2–0.4 MPa.
- **Electrical Contacts:**
  - Upper terminal: Wrapped 0.8 mm Cu wire secured with parafilm (no solder).
  - Lower terminal: Direct stainless-steel pin in mount.

## Pre-experiment Validation

To maximize the yield of functional in situ cells during synchrotron beamtime, prototype cells assembled with identical materials and protocols were systematically pre-tested under laboratory conditions. These pre-tests verified the expected electrochemical response (initial voltage profile, impedance and sealing integrity) and enabled early identification of failure modes such as short circuits. Due to the strict time constraints inherent to in situ synchrotron experiments, early identification of malfunctioning cells is critical. A system configuration, defined by parameters such as electrolyte amount, stack pressure, sealing method, separator layering, and electrode diameter, is considered sufficiently robust when at least four out of five identically assembled cells exhibit consistent electrochemical behaviour under cycling. This benchmark provides confidence in cell reliability and enables the development of a robust handling strategy and replacement protocol, minimizing beamtime loss and ensuring uninterrupted acquisition of high-quality data.

Representative cell voltage profiles of pre-test cells operated without imaging are shown in **Fig. S4**. Upon reaching the upper voltage cut-off and switching from constant-current to constant-voltage operation, the current decays only gradually, giving rise to an extended CV tail. Such behaviour is characteristic of the first formation cycle of Si-rich anodes, where extensive yet initially unstable solid–electrolyte interphase (SEI) formation drives continued electrolyte reduction and side reactions at constant potential. As a result, a fraction of the CV current is consumed by interphase growth [1]. The specific nano-SXCT cell geometry (~1 mm electrode diameter) and operating conditions further accentuate this response. The small active area and relatively high formation currents increase internal resistance, causing the voltage cut-

off to be reached early during CC charging and necessitating a prolonged CV hold to complete lithiation. Given the low absolute capacity of micro-scale cells, any parasitic leakage or self-discharge currents constitute a larger relative fraction of the applied current, so they can noticeably offset the net charging current and flatten the CV decay. These features are an intrinsic consequence of the strongly downscaled in situ cell design and limited beamtime and should be considered when comparing absolute electrochemical performance to larger-format industrial cells [1–4]. However, it still provides a representative platform to probe the chemo-mechanical behaviour of Si-rich anodes.

# Supplementary Note 3 – In Situ X-Ray Nano-Holo-tomography Measurement

Nano-holo-tomography scans were acquired at ESRF ID16B under an automatized and synchronized electrochemical protocol.

## Beamline & Imaging Parameters

- **Beamline:** ID16B, European Synchrotron Radiation Facility (ESRF), Grenoble, France[5].
- **Beamline Integration:** An overview of the integration of the in situ cell holder on the sample stage is presented in **Fig. S5**.
- **Beam Characteristics:** Pink beam ( $\Delta E / E = 10^{-2}$ ), conical X-ray beam at 29.6 keV; flux ~$10^{12}$ photons $s^{-1}$.
- **Holo-tomography:** Four phase-contrast tomography scans with slightly different propagation distances[6]. For each scan 2505 projections are recorded over 360°.
- **Detector:** PCO Edge 4.2 CMOS (2048×2048 px) coupled with 30 µm LSO scintillator; effective voxel size = 50 x 50 x 50 $nm^3$.
- **Projections:**
    - 2,505 projections per scan (angular step ≈ 0.143°; 360° total)
    - Exposure time: 20 ms/projection
    - 20 flat-field and 21 dark-field images per scan for correction
-

## Automated Electrochemical Protocol (RS232-Controlled)

A custom Python–LabView hybrid script communicated with the OGF500 potentiostat (firmware v2.3.1) which is synchronized with the holo-tomography acquisition software. The full logic (flowchart: **Fig. S6**) is as follows:

1. **Initialization:**
    - Record open-circuit voltage (OCV).
    - Set loop counter $n = 0$.
    - Define maximum scans ($N\_max$, based on beamtime or desired SoC intervals).
2. **Constant Current (CC) Phase:**
    - Apply C/3 until either:
        - Voltage ≥ 4.3 V, or

        - 30 minutes elapsed.
    - **Conditional Monitoring:** Using parallel logic gates, if $V \geq 4.3$ V before timeout, transition to CV phase. Otherwise, trigger a tomography scan, increment *n*, reset timer, and continue CC.
3. **Constant Voltage (CV) Phase (4.3 V Hold):**
    - Hold voltage at 4.3 V until either:
        - Current ≤ *I_threshold* (e.g., C/10), or
        - 30 minutes elapsed.
    - When condition met, trigger scan, increment *n*, reset timer. Continue CV if $n <$ *N_max*; otherwise, exit CC/CV loop.
4. **Discharge Phase:**
    - Discharge at C/6 to 2.5 V (lower cutoff).
    - Every 30 minutes, pause at OCV for scan; increment *n*, reset timer.
    - Once 2.5 V reached, pause at OCV and acquire two back-to-back scans (to capture relaxation effects).

**Synchronization & Pausing:**

- **Pre-Scan Pause:** One minute before each scan, the script sends a command to switch the cell to OCV.
- **Scan Duration:** ~13 minutes per holo-scan.
- **Post-Scan Resume:** Upon completion, script automatically switches potentiostat back to charging or discharging protocol.

Possible implications of pausing:
Pausing the charging during the tomographic scanning could lead to charge redistribution effects within the electrode, particularly in small-format cells where edge effects may transiently accelerate lithiation at the electrode periphery.

**Nomenclature in this experiment:**

- T0: no electrochemical dis-/charging (Pristine)
- T1, …, T6: during charging
- T7, T8 : during discharging
- T9: double scan

## Data Reconstruction & Processing

- **Phase Retrieval**: Paganin-like phase retrieval using a complex refraction index ratio $\delta/\beta = 170$ using the open-source software PyNX[7].
- **Filtered Backprojection Reconstruction**: ESRF software Nabu[8].
- **Ring Artifact Reduction & Histogram Equalization**: Post processing ring correction matlab algorithm based on image filtering[9]. And histogram equalization applied via scikit-image's exposure.equalize_hist function to enhance contrast between Si and pore phases.

# Supplementary Note 4 - Machine-Learning Image Segmentation

Segmentation distinguishes Si and pore, electrolyte, conductive binder domain (CBD) phases using two attention residual U–Net models.

## Model Architecture & Training

- **Architecture:** Attention residual U–Net[10–12] (Keras v2.10.0, TensorFlow v2.10.1), featuring:
  - Residual connections for improved gradient flow
  - Attention gates at each skip-connection to focus on relevant features
  - Batch normalization and dropout (p = 0.2) for stability and regularization
- **Data Preparation:**
  - **Models:** Model 1 (T0-T2); Model 2 (T3-T8).
  - **Training Images:** 12 manually annotated 2D slices per model (size: 256×512 px) created in Ilastik (v 1.4.0b14)[13].
  - **Label Classes:** 2 classes (Si and background (pore, electrolyte, SEI, CBD).
  - **Augmentation (Albumentations v1.4.18):** Each slice underwent three random transformations:
    A.HorizontalFlip(p=0.5),
    A.RandomScale(p=0.5),
    A.ElasticTransform(alpha=30, sigma = 50, p=0.3),
    A. Affine(shear=(-10, 10), p=0.3),
    A.Affine(rotate = (0, 20), p = 0.3)

    **Resulting Dataset:** 48 augmented images per model.
- **Hyperparameters:**
  - Input shape: (256, 512, 1)
  - Batch size: 1
  - Epochs: 150
  - Optimizer: Adam (lr = $1\times10^{-4}$)
  - Loss: Binary_crossentropy
  - Activation function: relu
  - Decoder block type: upsampling, attention gating, residual connections
  - Validation split: 30%
  - Hardware: NVIDIA RTX A5000 GPU (CUDA v12.4)

# Supplementary Note 5 - Strain Analysis with SPAM (Software for Practical Analysis of Materials)

We employed the Software for Practical Analysis of Materials (SPAM)[14] to quantify full-field displacement and strain maps within electrode volumes across sequential tomographic scans.

## Workflow Overview (Fig. S7)

1. **Image Pair Acquisition:** For timesteps T0–T9. Each image pair (T_i, T_{i+1}) forms the input to the registration pipeline.
2. **Eye Registration:**
    - Manual rapid, approximate alignment to correct for global rigid body shifts at the centre of mass of the electrode.
3. **Non-Rigid Registration:**
    - Automatic optimization of the transformation at the centre of mass of the electrode (12 DOF: rotation, normal strain, shear strain, translation)
    - Iteration parameters: max_iters = 3000; convergence tol = $1\times10^{-4}$.
    - Upon convergence, proceed to Local-DIC.
4. **Local-Digital Image Correlation (LDIC):**
    - Hierarchical node spacing: [100, 70, 35] pixels.
    - For node_spacing = 100vx: compute initial deformation field $\Phi_1$. If For non-converged nodes, filter based on the 9 converged neighbours, and interpolate the filtered field $\Phi_1$' to node_spacing = 70vx .
    - Repeat for node_spacing = 70 → $\Phi_2$, filter then interpolate to node_spacing = 35 → repeat an LDIC run with the interpolated filtered field as input for $\Phi_3$ final.
    - Filtering the non converged nodes of the final field $\Phi_3$
    - If any stage fails (majority of non converged nodes), repeat with adjusted parameters (margin (10/ 20/ 30/ 40), number of iterations: 1000/ 2000/ 3000)
5. **Multiplicative Phi-Field Analysis:**
    - Compute cumulative transformation for e.g. T0→T2 by applying $\Phi_{12} \circ \Phi_1$.
    - In general, $\Phi_i = \Phi_{i,i-1} \circ \ldots \circ \Phi_{12} \circ \Phi_1$.
6. **Strain Tensor Calculation:**
    - From displacement field $\Phi$, compute strain tensor.
    - Calculate volumetric strain ($\varepsilon$).
    - Output strain maps as 3D images (.tif) and as numerical arrays (.csv).
7. **Residual mapping:**
    - Multiplicative deformation fields ($\Phi$) are used to deform reference image to match specific timestep (T0 → Ti_def, i = 1, …, 9)
    - Calculate residual image for specific time step: Ti - Ti_def

# Supplementary Note 6 - Field Emission Scanning Electron Microscopy (FESEM)

1. **Cell disassembly**: The battery cell is first disassembled in an Ar-filled glove box ($O_2$ and $H_2O$ levels < 1 ppm) (This step is only necessary for in situ anode analysis).
2. **Anode drying:** The anode is left in the glove box for 24 hours, facilitating the evaporation of any residual electrolyte (This step is only necessary for in situ anode analysis).
3. **Cross-section cutting:** The anode is mounted on a SEM specimen stub using silver conductive paste. Cross-sectioning is performed using a Hitachi IM4000+ ion milling system.
4. **FESEM investigation:** Imaging is performed using a ZEISS GeminiSEM 450 operated under the following conditions:
   - Acceleration voltage: 5 kV
   - Probe current: 3 nA
   - Working distance: 8.3 / 8.5 mm
   - Pixel size: 186.1 nm; 18.61 nm; 5.582 nm;
5. **Energy-dispersive X-ray spectroscopy (EDS):** EDS analysis is performed with an Oxford Ultim Extreme detector.
   - Acceleration voltage: 3 kV
   - Probe current: 3 nA
   - Image size: 1024 × 768 pixels

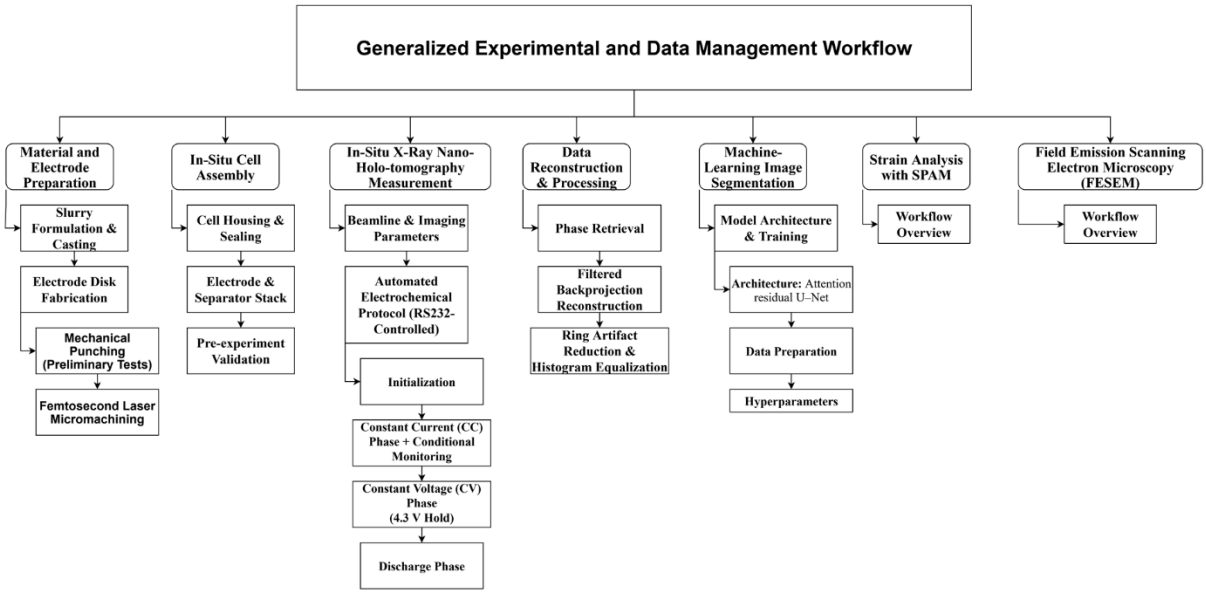


**Figure S1:** Experimental and data management workflow.

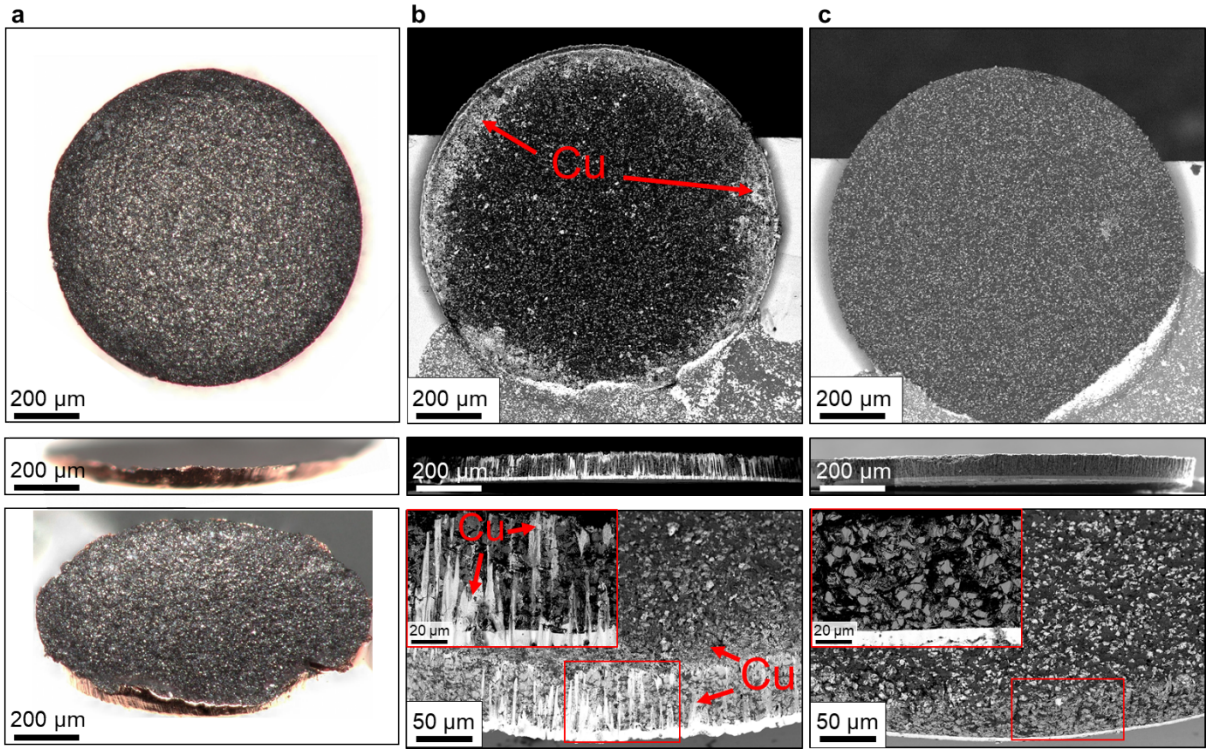


**Figure S2:** Comparison of electrode preparation techniques for circular electrodes, viewed from the top (upper row), side (middle row), and at a tilted angle (bottom row). (a) Light microscopy images of a mechanically punched electrode showing significant edge tearing, deformation of the copper foil, and non-uniform geometry. (b, c) BSE-FESEM images of electrodes prepared via femtosecond laser micromachining. (b) Laser cutting from the copper side results in visible copper redeposition at the electrode edge and along the silicon anode's sidewall. (c) Cutting from the silicon side avoids redeposition, yielding a clean and sharply defined electrode. Insets in (b) and (c) show magnified views of the electrode edge highlighting the presence or absence of copper redeposition.

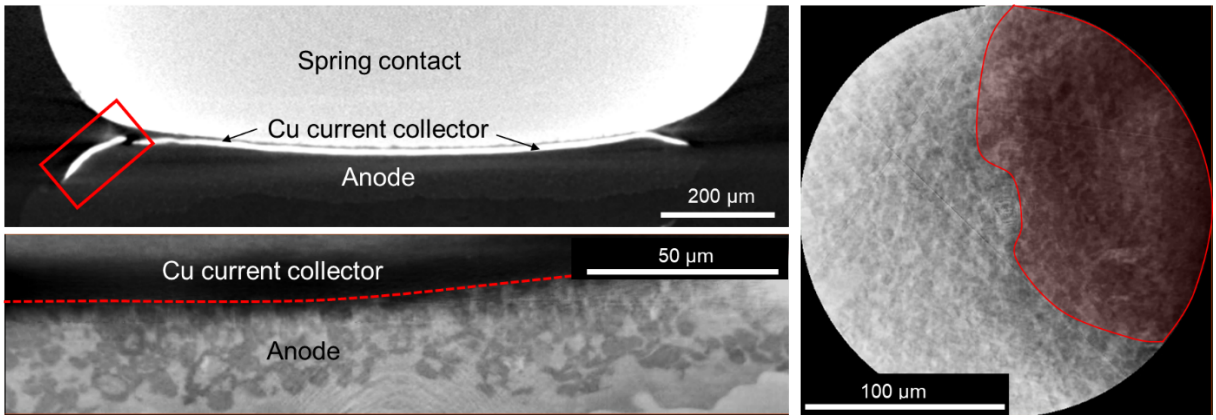


**Figure S3:** X-ray tomographic slice images illustrating typical artefacts encountered during imaging. The top-left panel shows edge-tearing of the copper foil (mechanical punching), while the bottom-left highlights contrast gradients resulting from non-flat, bent electrode geometries. These structural irregularities introduce X-ray scattering artefacts and contrast variations, as evident in the nano-SXCT slice image on the right.

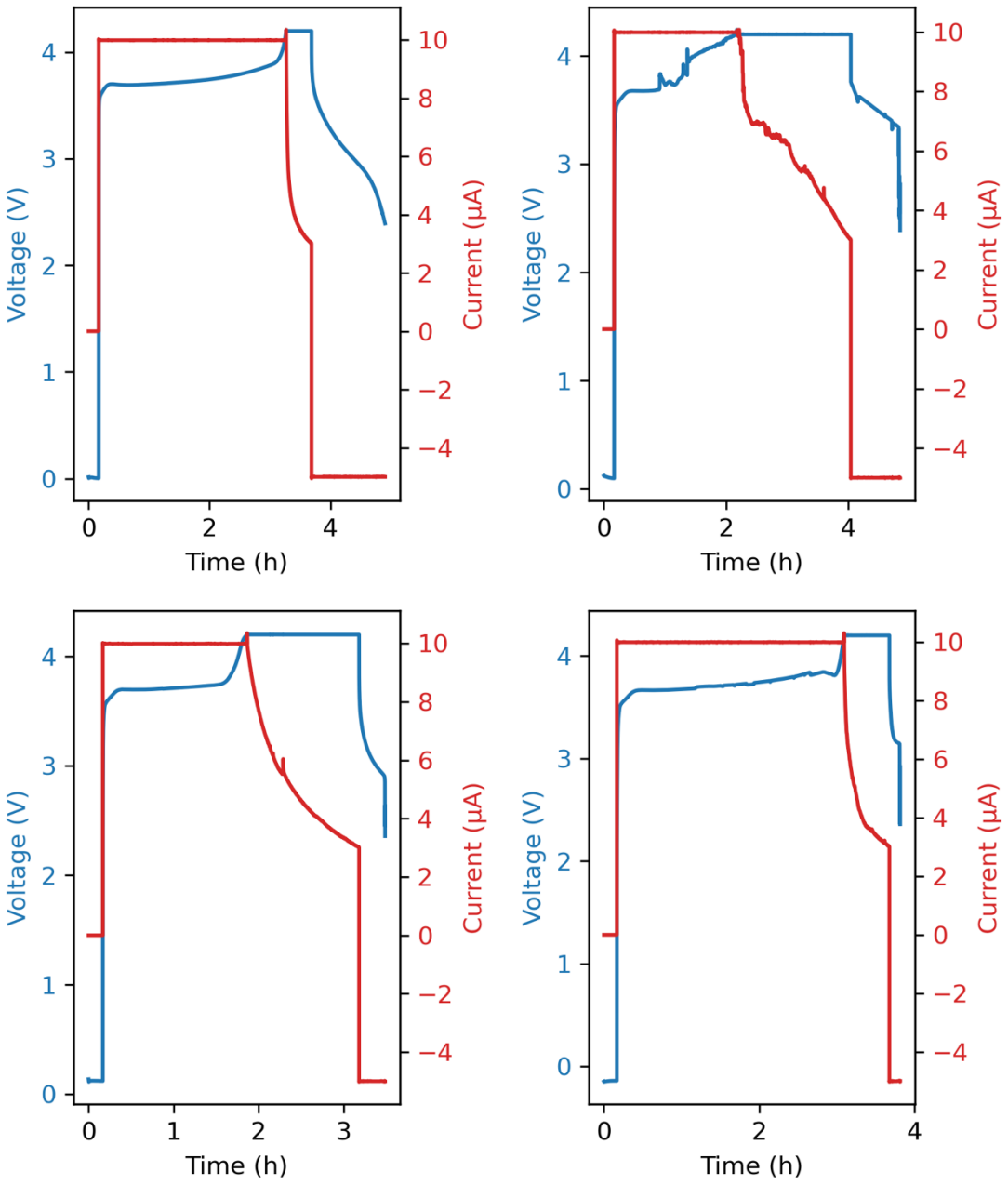


**Figure S4:** Voltage profiles of test cells charged (without imaging) at a C-rate of C/3 using a constant-current (CC) step up to 4.3 V, followed by a constant-voltage (CV) hold until the current dropped below C/10 and subsequently discharged to 2.5 V.

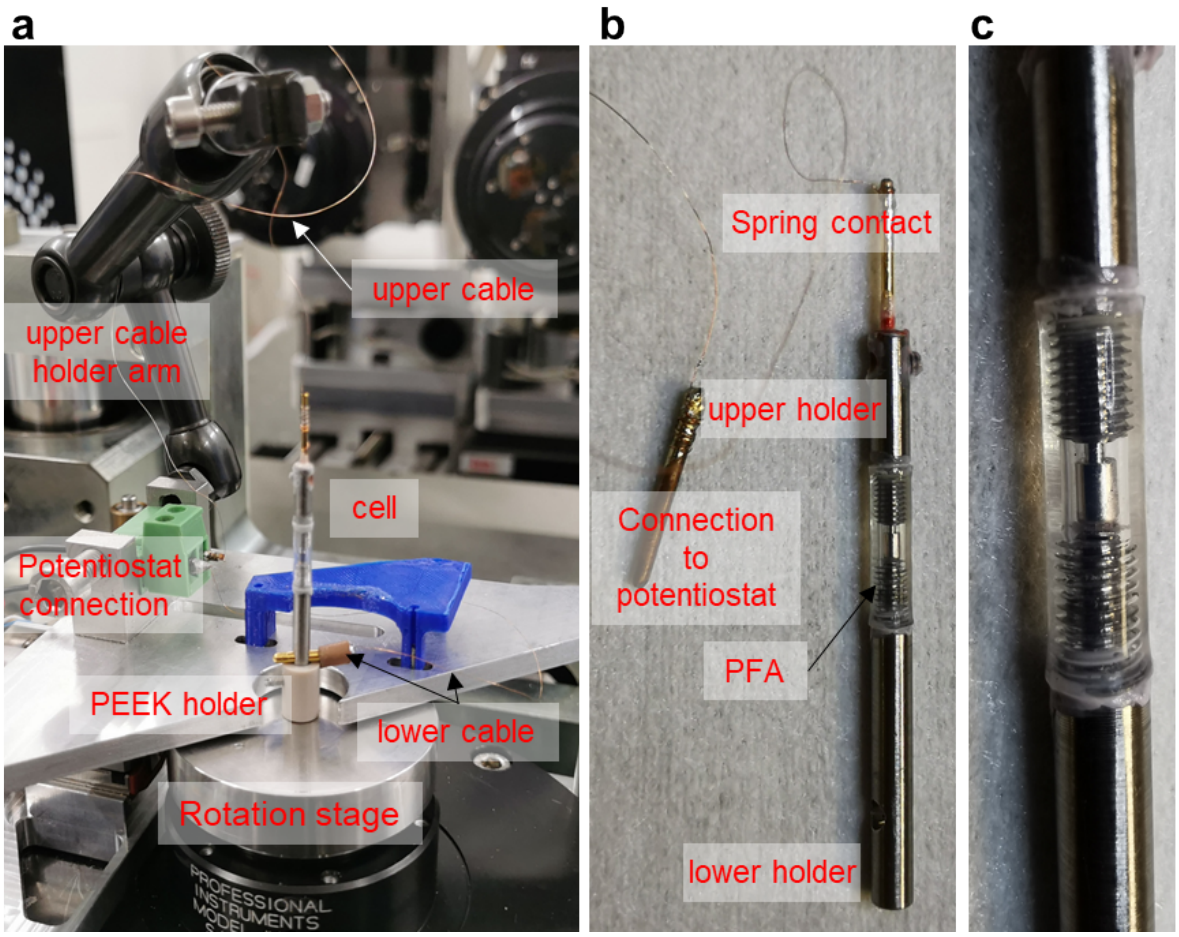


**Figure S5:** Overview of the sample stage and custom in situ cell holder. (Left) Sample stage at the ID16B beamline equipped with attachments for in situ measurements. (Middle) Custom-designed electrochemical cell holder enabling controlled application of external pressure during operation. (Right) Close-up view of the assembled holder, highlighting the PFA tubing, upper and lower stainless-steel threaded mounts, and the spring-loaded contact ensuring reliable electrical connection to the LIB cell. All component interfaces are sealed with lacquer to ensure airtightness.

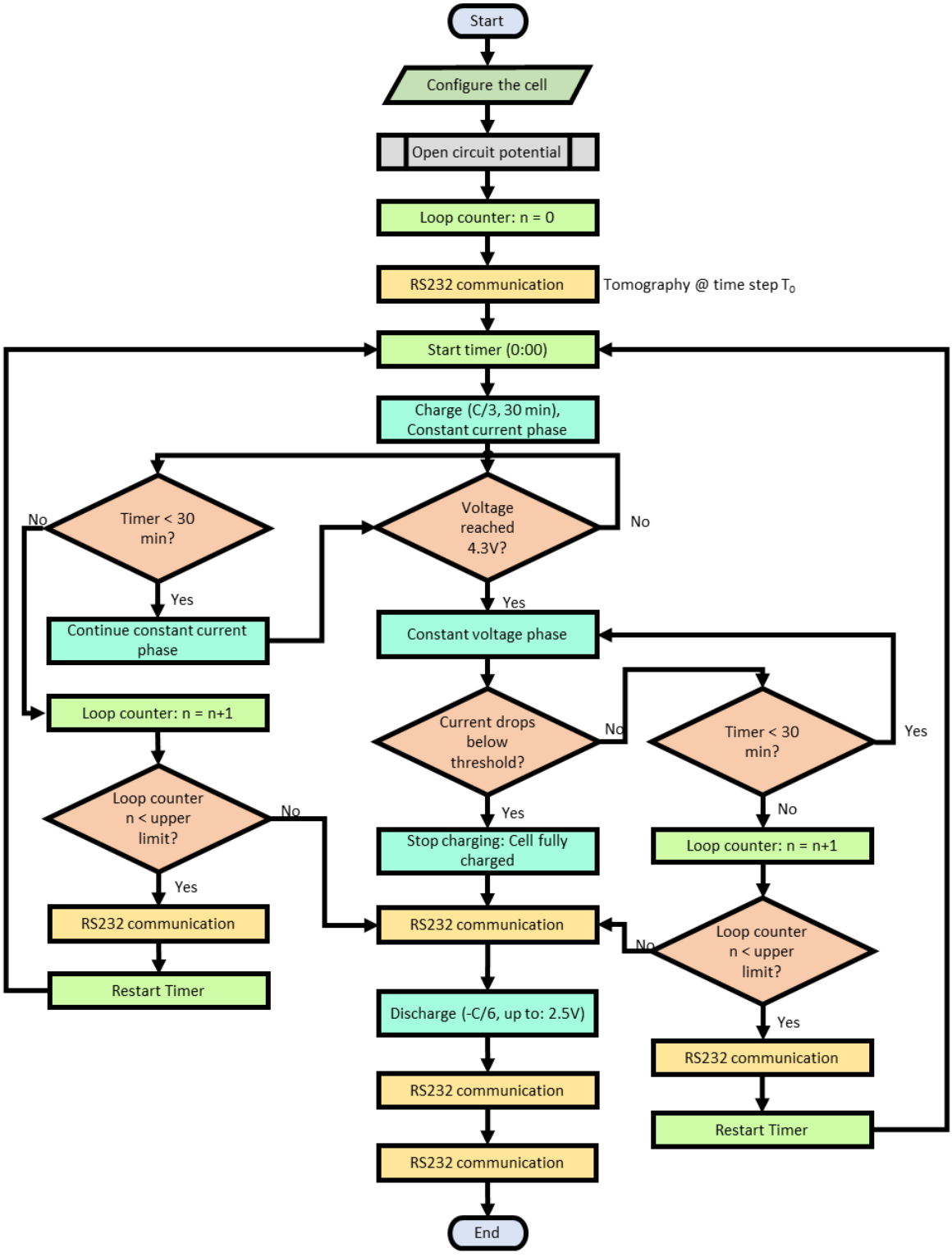


**Figure S6:** Flowchart of automation for in situ X-ray nano-holo-tomography

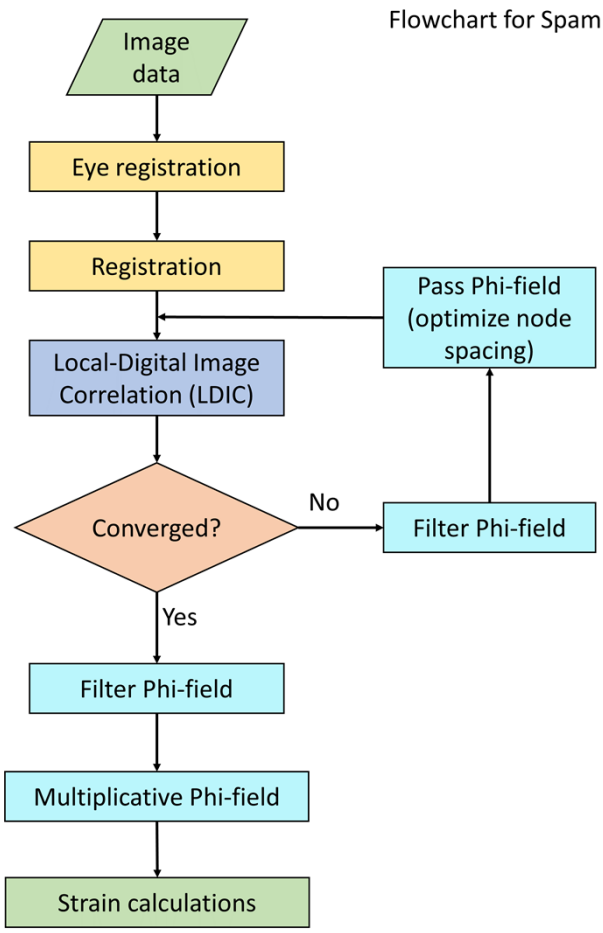


**Figure S7:** Workflow for SPAM: Progressive multi-frame analysis for material deformation characterization

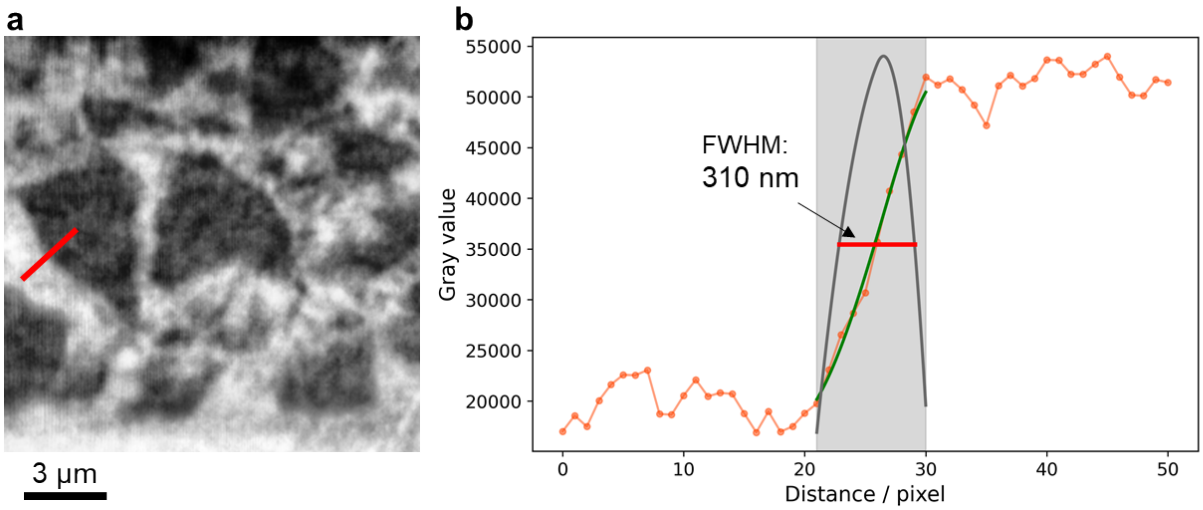


**Figure S8:** Intensity profile (grey values) extracted along the red line, used to calculate spatial resolution. **a** A representative line profile orthogonal to a particle edge is extracted. **b** Spline interpolation (green curve) is applied to the raw intensity profile (orange) to produce a smooth representation of the edge transition. The derivative of the spline fit (black line) highlights the intensity gradient at the edge. The full width at half maximum (FWHM) of this derivative peak, marked by the red line, is used to quantify the spatial resolution. The FWHM, initially measured in pixels, is converted to nanometres using the voxel size (50 x 50 x 50 $nm^3$). Averaging results from 10 different particle edges across 10 different particles at timestep T0 yields a spatial resolution of 307 ± 15 nm.

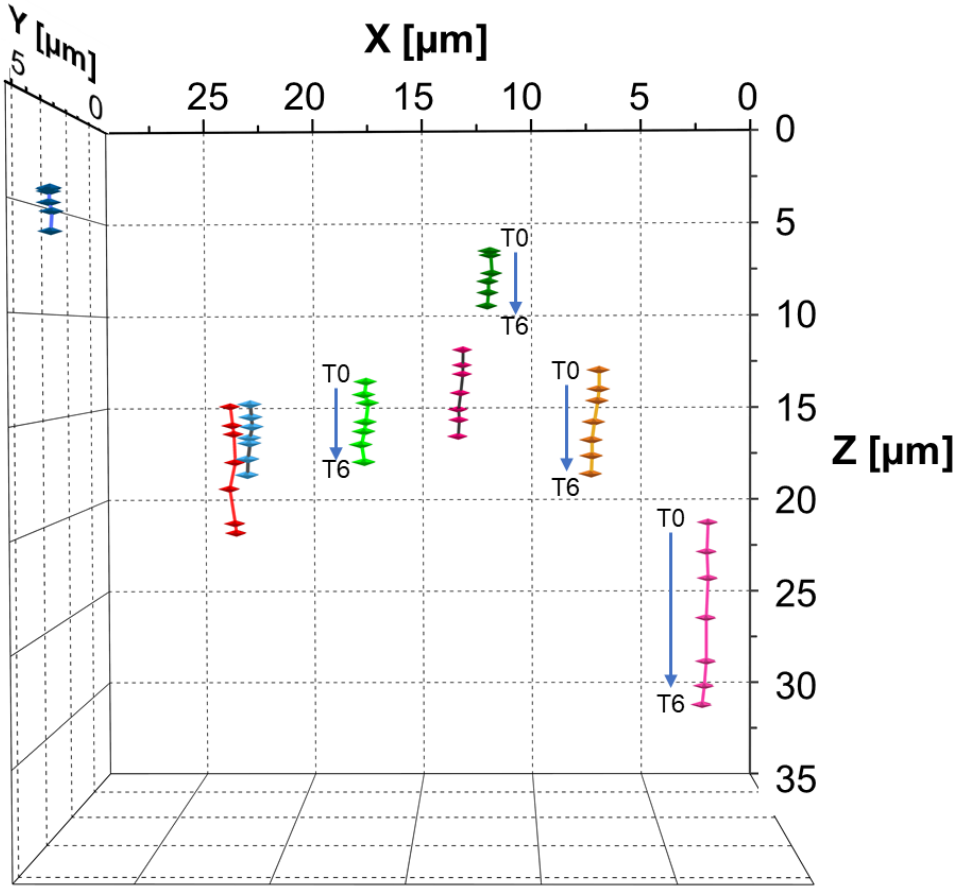


**Figure S9:** Axial displacement trajectories of individual silicon particles during lithiation (T0–T6). Particle positions are tracked relative to their initial coordinates at T0. Z = 0 corresponds to the current collector interface. Particles located closer to the separator exhibit significantly larger axial displacements compared to those near the current collector, indicating spatially heterogeneous mechanical responses across the electrode thickness. The observed motion is predominantly in the axial (z) direction, while lateral displacements (x, y) remain within the estimated uncertainty range. Tracking is performed by calculating the centre of mass of the non-lithiated phase of each particle, based on image segmentation using the ML-based approach.

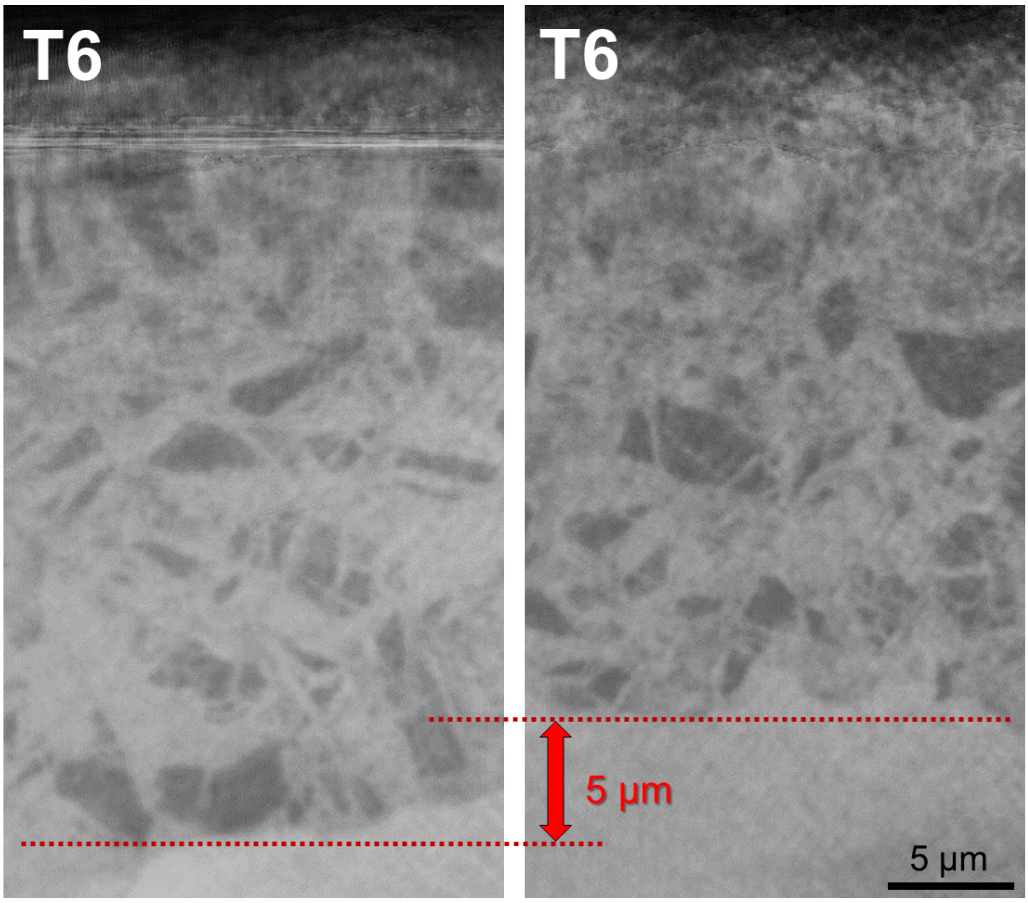


**Figure S10:** Representative nano-SXCT transversal slices from the reconstructed volume of the anode at the charged state T6 at two different positions highlighting local variations in thickness.

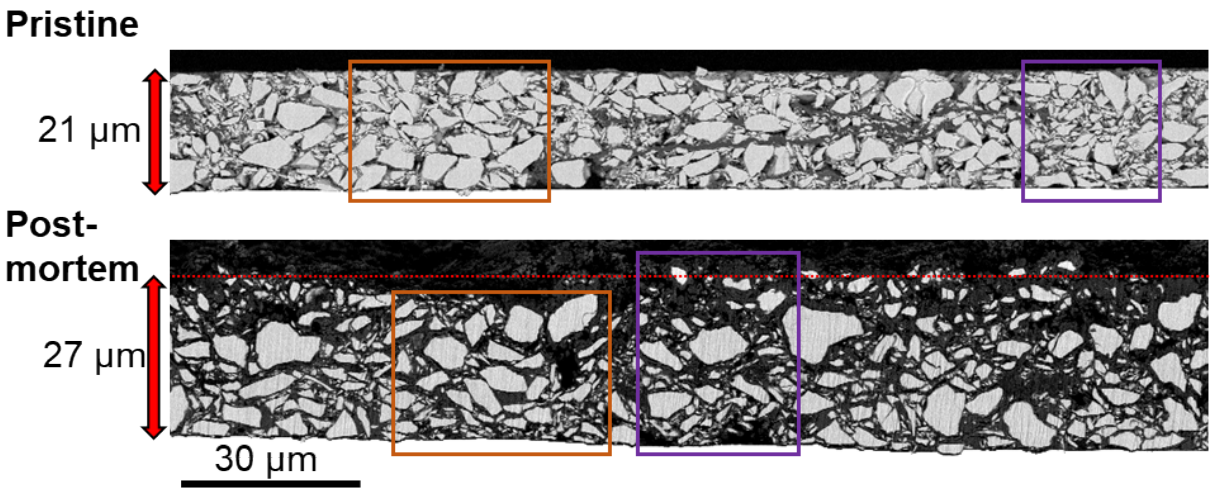


**Figure S11:** Cross-sectional BSE-FESEM of the pristine anode and the post-mortem anode after one cycle within the in situ experiment. The pristine electrode shows a relatively uniform thickness (~21 µm), with minor heterogeneities such as binder-rich zones and local porosity, which may later influence spatial variations in strain development. A region containing a cluster of larger silicon particles is marked with an orange box, while a region containing smaller particles is highlighted in purple, illustrating the spatial variation in particle morphology within the same electrode cross-section. The post-mortem electrode exhibits an average thickness of ~27 µm. Local variations (25–29 µm) reflect inhomogeneities in particle size distribution, binder content, and porosity.

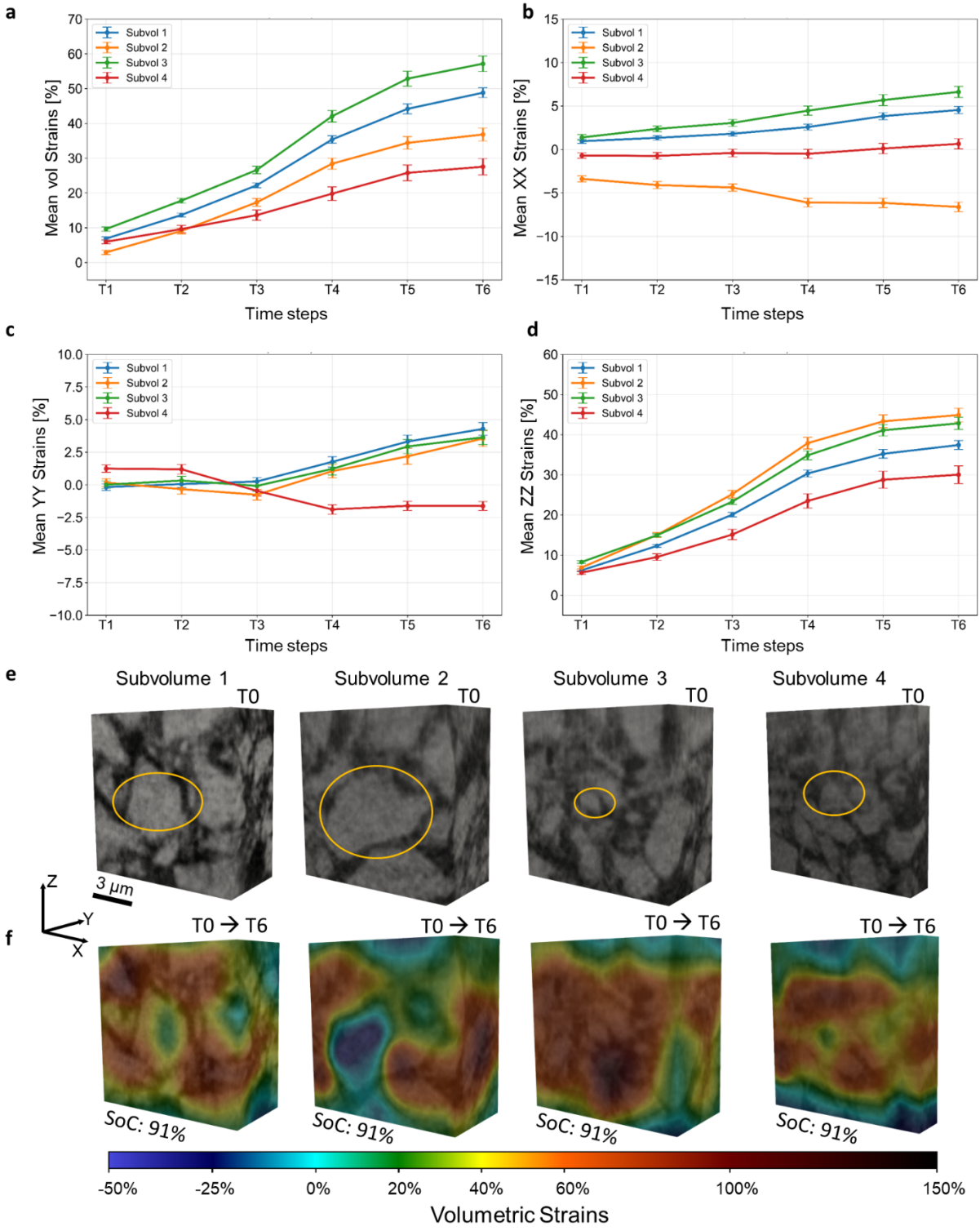


**Figure S12:** Temporal evolution of volumetric strains and axial strains within four selected volumes of interest (VOIs) as shown in **a, b, c** and **d**, measuring 15 × 15 × 15 µm³ and 15 × 15 × 10 µm³ as shown in **e**. The VOIs are centred on the centre of mass of a representative silicon (Si) particle, as visualized in the central tomographic slice of each subvolume. The central reference particle in each VOI is highlighted in orange. Volumetric strain is computed relative to the pristine state (T0) as shown in **f**.

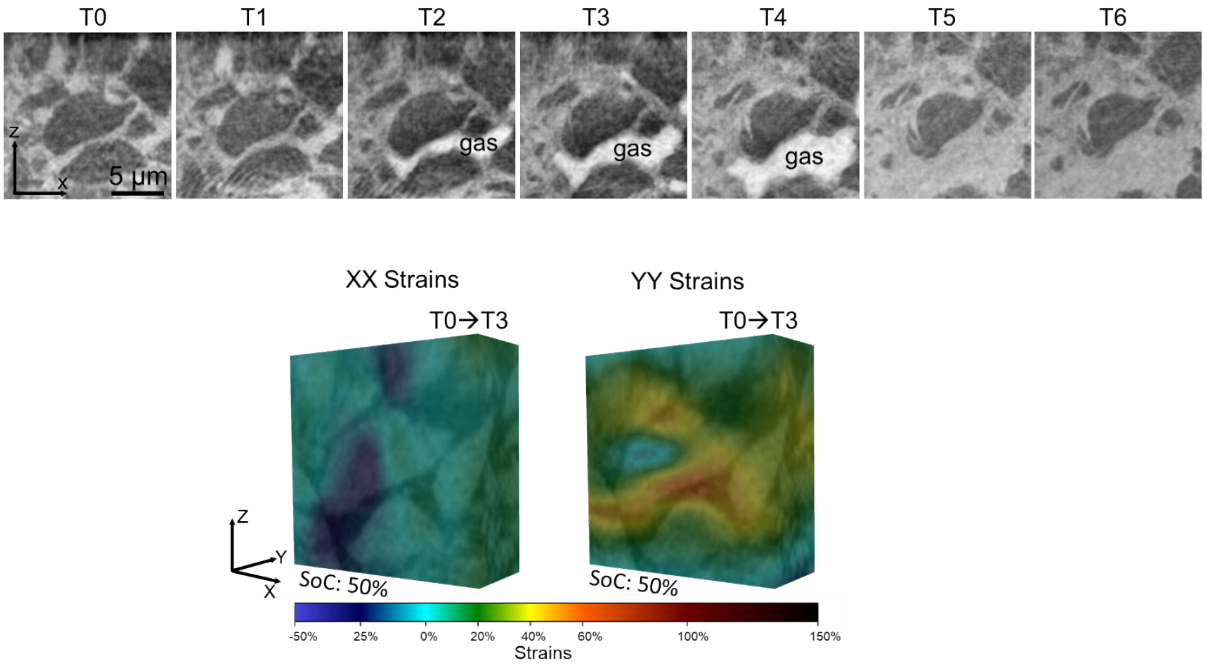


**Figure S13:** Transient gas bubble formation during lithiation (T0–T6). Representative nano-SXCT slice images of the same electrode region reveal the evolution of a transient gas bubble in the pore space beneath a large central silicon particle (dark grey) as shown in **a**. Between T1 and T2, a distinct low-density feature emerges, indicative of gas formation. The bubble continues to expand until T4, after which it disappears in T5, becoming indistinguishable from the surrounding carbon binder domain (CBD), solid electrolyte interphase (SEI) and electrolyte-filled pore space. In order to investigate the effects of gas bubble on strains, as shown in **b** the axial strains are plotted. This demonstrates that strains in X-direction are compressive and tensile in Z-direction.

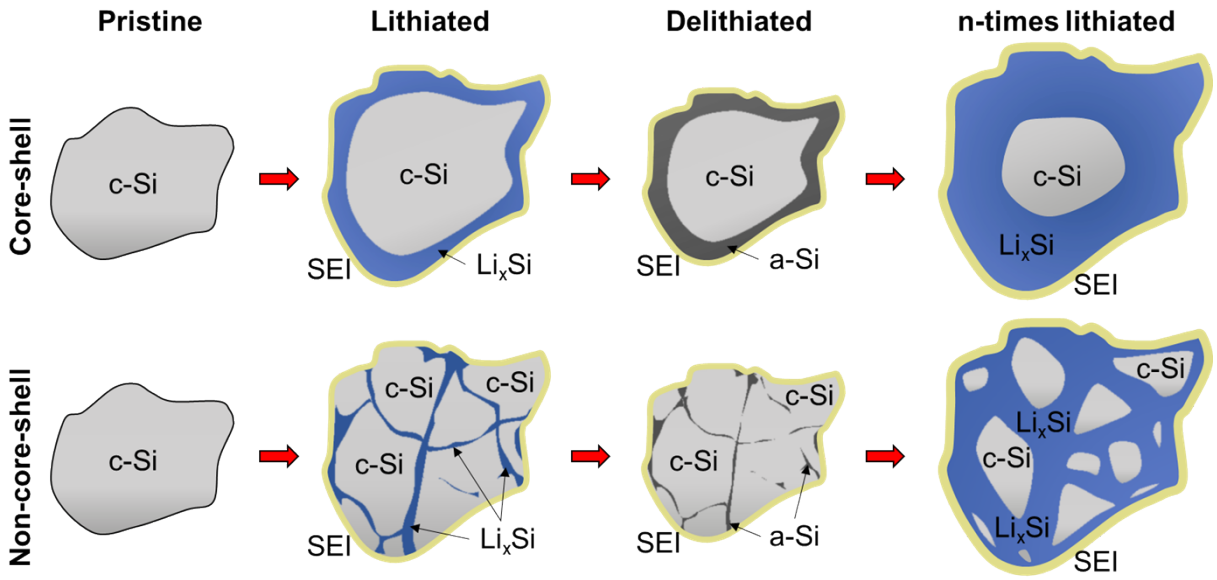


**Figure S14:** Schematic illustration of the classical two-phase core–shell lithiation mechanism (top row) and the non–core–shell lithiation behaviour (bottom row) in crystalline silicon particles. In the core–shell picture, a crystalline Si particle initially undergoes partial lithiation, forming an outer amorphous lithiated shell ($Li_xSi$) surrounding an unreacted crystalline core, while a solid–electrolyte interphase (SEI) forms at the particle surface. During delithiation, Li is extracted and transported back to the cathode, leaving an amorphous Si shell while the crystalline core remains intact. With continued cycling and deeper lithiation, an increasing fraction of the crystalline core is converted, and eventual full lithiation may occur, accompanied by large volume expansion and further SEI growth. In contrast, in the non–core–shell picture, lithiation proceeds along internal pathways that span across the particle, penetrating the crystalline core. As a result, even during the first lithiation, regions within the particle interior participate in the alloying reaction. Upon delithiation, Li is extracted but amorphous bands and regions persist within the particle. With repeated lithiation, these amorphous bands expand and interconnect, while the remaining crystalline Si domains progressively shrink.

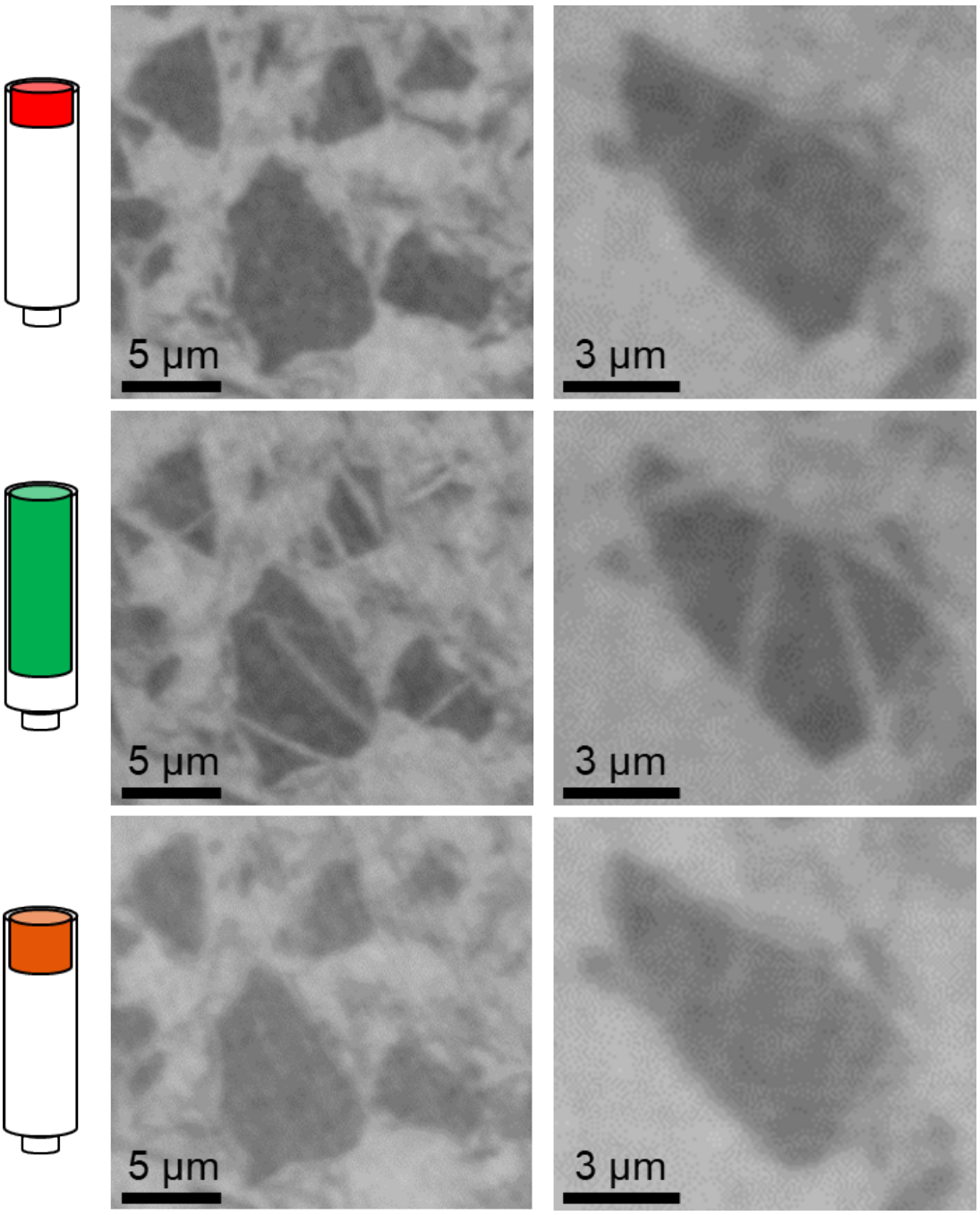


**Figure S15:** Zoomed-in on representative silicon particle regions in the reference cell across different electrochemical states. Tomographic slice images show a cluster of silicon particles (left) and a single silicon particle (right). The top row shows the pristine, uncycled state, showing homogeneous grey values with no internal features or contrast variations. The middle row represents a charged state, where distinct bright pathways emerge across the particle volumes, indicating the formation of low-density, lithiated regions during electrochemical cycling. The bottom row shows a discharged state, where these pathways have disappeared again and the internal contrast returns to a state similar to the pristine condition. Nonetheless, subtle grey-value variations remain, suggesting minor persistent structural or compositional changes.

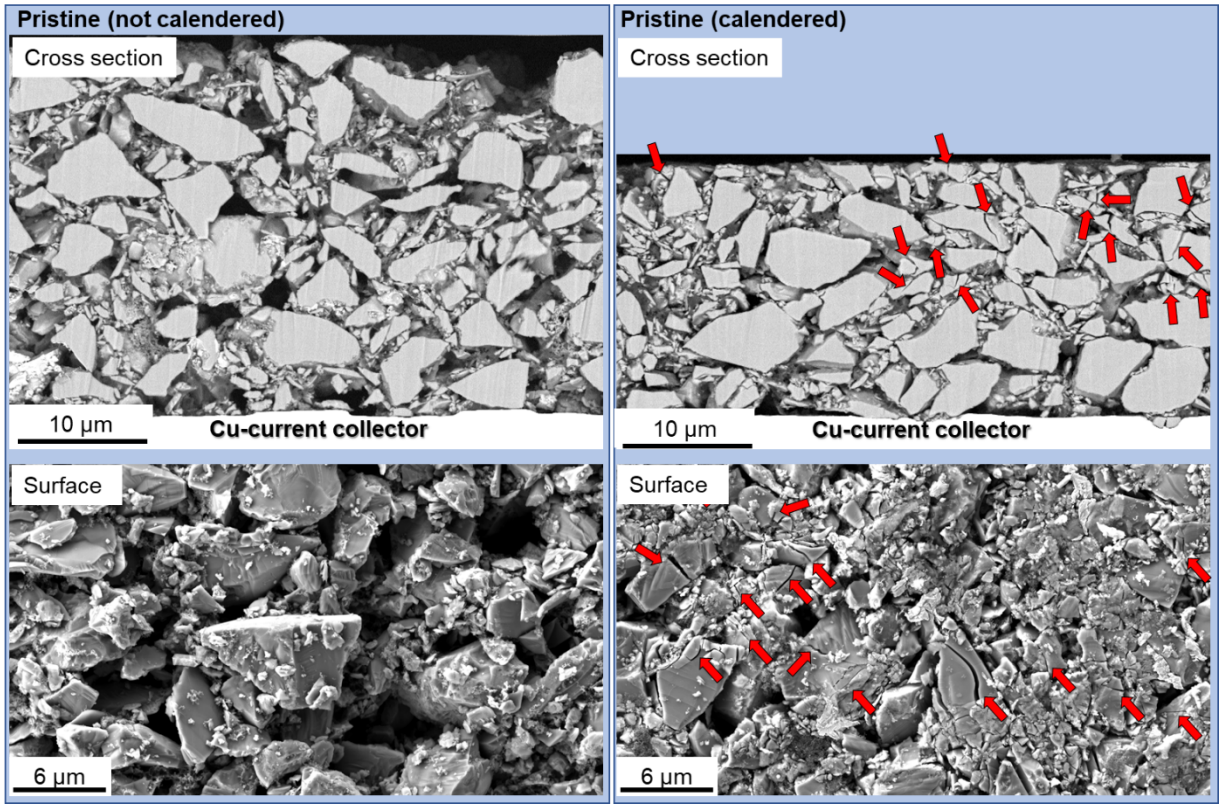


**Figure S16**: Effect of electrode calendering on silicon particle integrity. The left column shows the pristine electrode coated onto a 10 µm thick copper foil using the doctor blade technique, while the right column displays the same electrode after calendering, resulting in a final thickness of approximately 20 µm. Top images present cross-sectional images acquired via backscattered electron (BSE) FESEM imaging. In the as-coated (non-densified) electrode, silicon particles appear intact, with no detectable internal cracking. In contrast, the calendered electrode exhibits a high fraction of cracked particles, particularly near the surface adjacent to the calender roll (some examples marked with red arrows). Bottom images compare the electrode surfaces before and after calendering. The as-coated electrode surface shows undamaged particles, while the densified electrode surface reveals extensive particle breakage, confirming that mechanical compression during calendering induces significant damage, predominantly in the topmost layer.

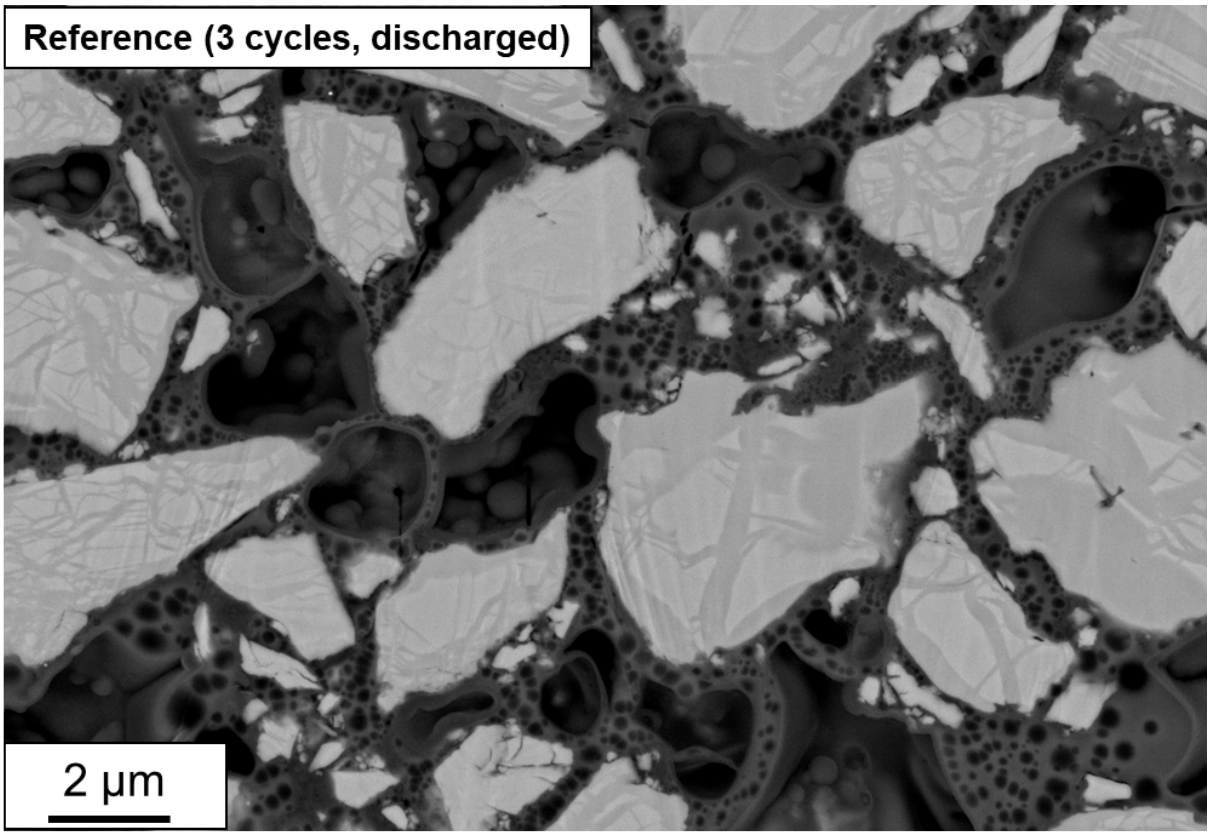


**Figure S17:** Cross-sectional BSE-FESEM image of a pouch format reference cell in the delithiated state after three full cycles. Multiple silicon particles of varying sizes are visible. Darker grey features traverse the particles, segmenting them into brighter regions or islands. These internal contrast variations, indicative of previously lithiated pathways, are observed not only in larger particles (>3 µm) but also in smaller ones, suggesting that this phenomenon occurs broadly across particle sizes and shapes. Test protocol reference cell: The cell is cycled between 2.5V (lower cut-off voltage) and 4.2V (upper cut-off voltage). The procedure begins with charging and discharging at 0.1C, followed by two consecutive cycles of charge and discharge at a higher rate of 0.33C.

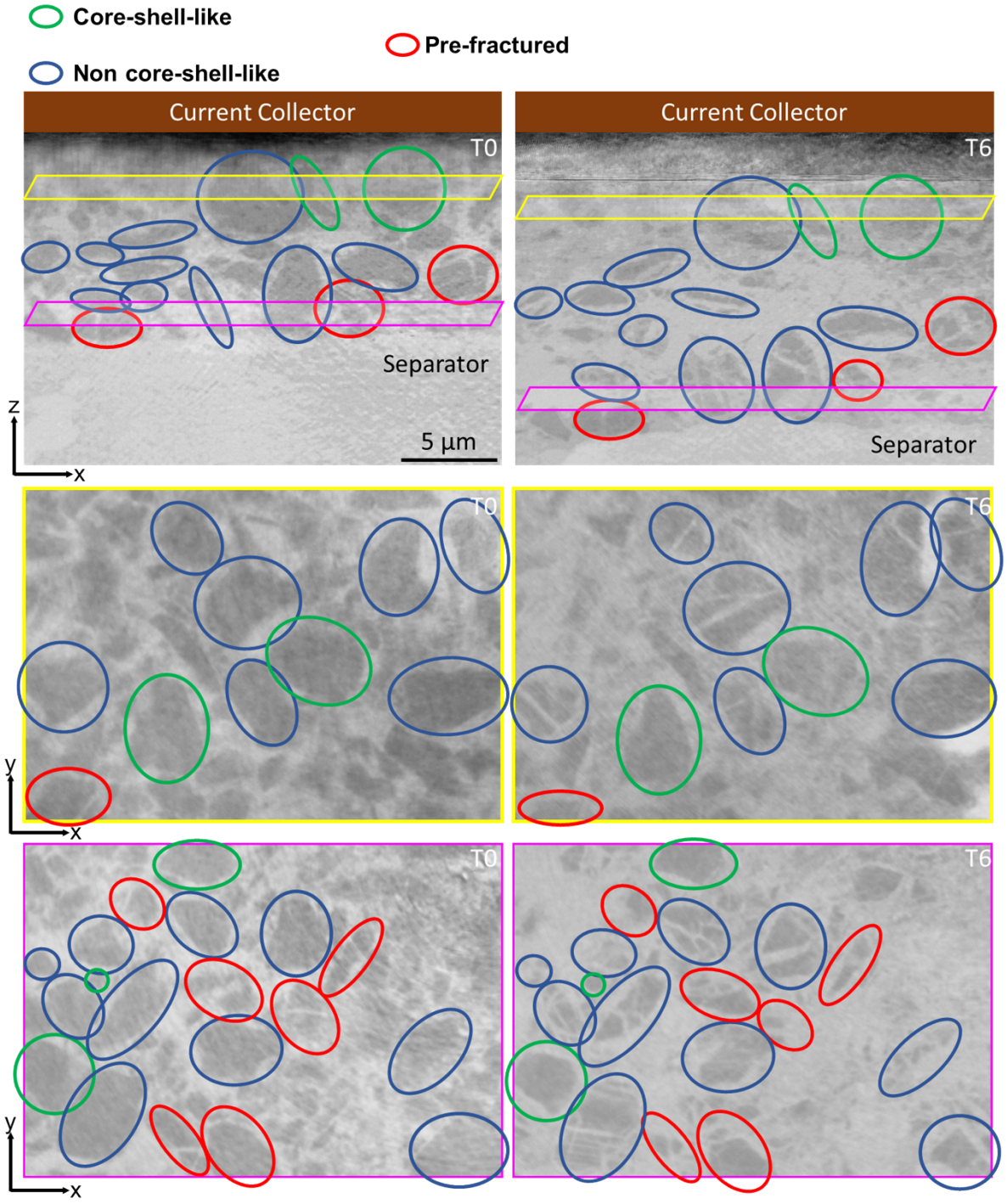


**Figure S18**: Particle responses to lithiation. Exemplarily visualized on a region from reconstructed slices within the nano-SXCT volume for the pristine (T0) and charged (T6) timesteps. While only small regions within a few slices (xz; xy) are displayed here for illustrative purposes, the actual analysis was comprehensively performed manually over all slices and the entire volume.

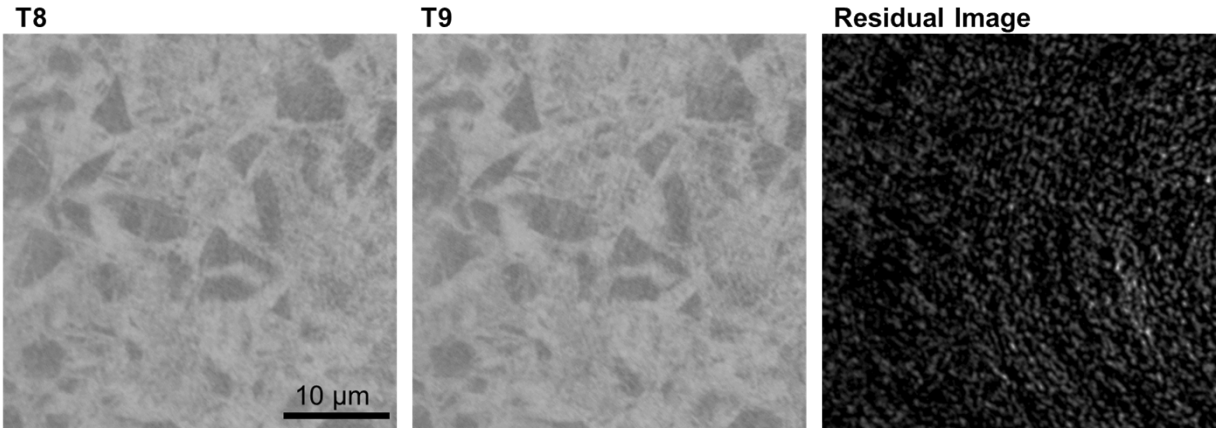


**Figure S19:** Double-scan comparison between T8 and T9. Left: scan T8; middle: scan T9; right: residual image obtained by subtracting T8 from T9 for a representative slice. Only minor differences are observed (bright spots), which can be attributed to noise, indicating negligible structural changes between the two scans. To quantify this noise, LDIC analysis is performed between T8 and T9 using the same correlation windows as the volume investigated in the main text. The T8 image is first deformed to match T9 after applying Phi field obtained through this LDIC process. Afterwards, the residual image is obtained by subtracting the deformed T8 from T9, followed by applying a Gaussian blur with a sigma of 2 and processing the image with the absolute value function in ImageJ. The resulting residual values of 5000 grey value provide a baseline measure of noise, threshold used for residual analysis on the volumes in this study.

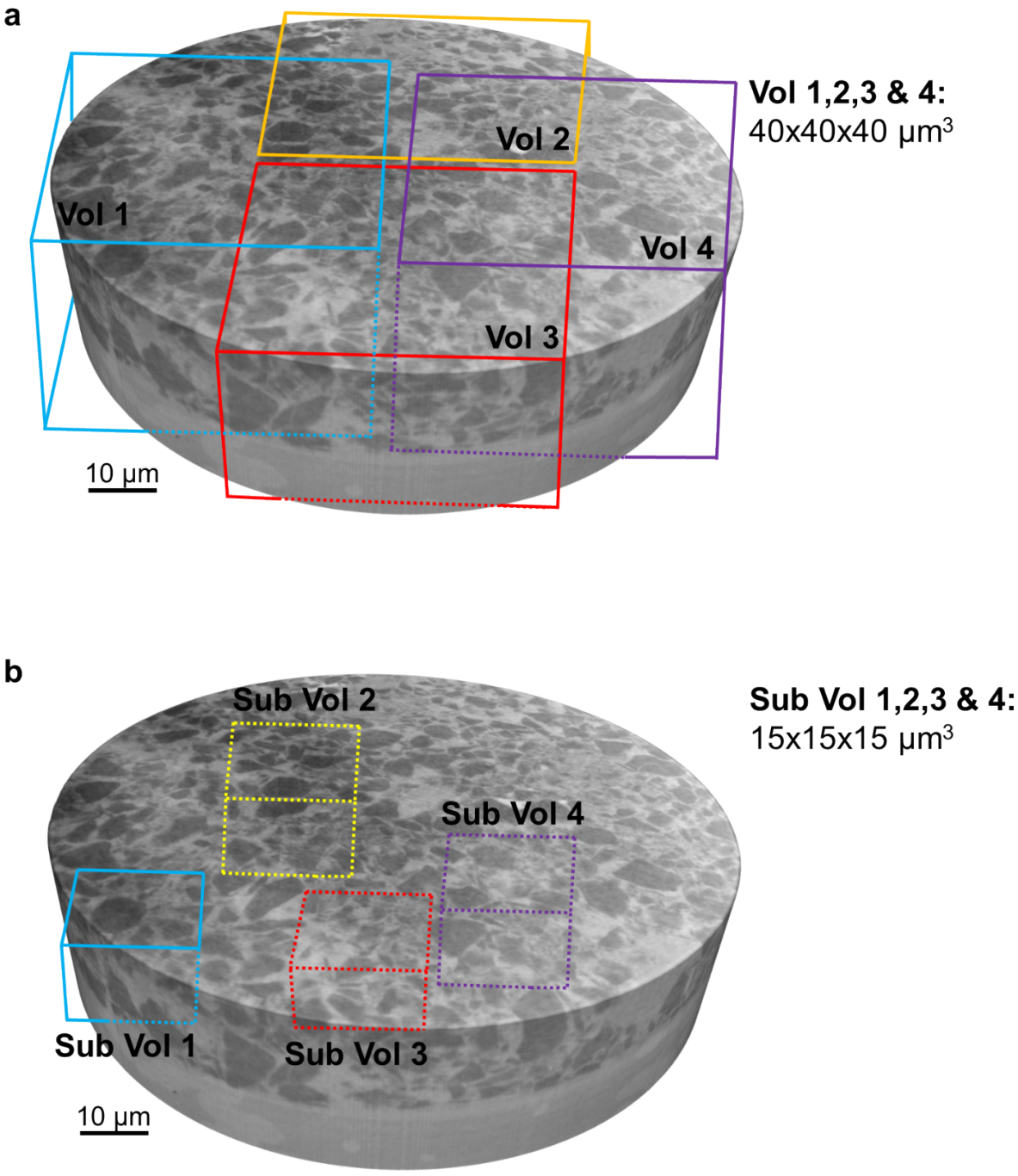


**Figure S20: a** Overview of selected regions used for electrode-scale analysis. The four VOI insets labelled "Vol 1", "Vol 2", "Vol 3" and "Vol 4" represent distinct 40x40x40 µm³ regions of interest selected for detailed analysis. **b** Overview of selected regions used for local strain analysis (particle-centred frame).

# Supplementary References


1 F. Schomburg, B. Heidrich, S. Wennemar, R. Drees, T. Roth, M. Kurrat, H. Heimes, A. Jossen, M. Winter, J. Y. Cheong and F. Röder, *Energy Environ. Sci.*, 2024, **17**, 2686–2733.

2 C. Tan, S. R. Daemi, O. O. Taiwo, T. M. M. Heenan, D. J. L. Brett and P. R. Shearing, *Materials 2018, Vol. 11, Page 2157*, 2018, **11**, 2157.

3 L. Su, P. Choi, B. S. Parimalam, S. Litster and B. Reeja-Jayan, *MethodsX*, 2021, **8**, 101562.

4 R. G. Scurtu, A. Innocenti, V. Scheck, M. Maunz, T. Waldmann, M. Hölzle, A. Hoffmann, P. Axmann and M. Wohlfahrt-Mehrens, *Nat. Nanotechnol.*, 2025, **20**, 970–976.

5 G. Martinez-Criado, J. Villanova, R. Tucoulou, D. Salomon, J.-P. Suuronen, S. Labouré, C. Guilloud, V. Valls, R. Barrett, E. Gagliardini, Y. Dabin, R. Baker, S. Bohic, C. Cohen and J. Morse, *J. Synchrotron Radiat.*, 2016, **23**, 344–352.

6 P. Cloetens, W. Ludwig, J. Baruchel, D. Van Dyck, J. Van Landuyt, J. P. Guigay and M. Schlenker, *Appl. Phys. Lett.*, 1999, **75**, 2912–2914.

7 V. Favre-Nicolin, G. Girard, S. Leake, J. Carnis, Y. Chushkin, J. Kieffer, P. Paléo and M.-I. Richard, *J. Appl. Crystallogr.*, 2020, **53**, 1404–1413.

8 P. Paleo, J. Lesaint, H. Payno, A. Mirone, N. Vigano and C. Nemoz, *Zenodo*, 2024, preprint, DOI: 10.5281/zenodo.11104029.

9 A. Lyckegaard, G. Johnson and P. Tafforeau, *International Journal of Tomography & Statistics*, 2011, **18**, 1–9.

10 O. Ronneberger, P. Fischer and T. Brox, eds. N. Navab, J. Hornegger, W. M. Wells and A. F. Frangi, Springer International Publishing, Cham, 2015, pp. 234–241.

11 M. Häusler, R. Wilhelmer, R. J. Sinojiya, O. Stamati, J. Villanova, C. Stangl, S. Koller and R. Brunner, *J. Mater. Chem. A*, 2025.

12 F. F. Chamasemani, F. Lenzhofer and R. Brunner, *Sci. Rep.*, 2024, **14**, 21279.

13 S. Berg, D. Kutra, T. Kroeger, C. N. Straehle, B. X. Kausler, C. Haubold, M. Schiegg, J. Ales, T. Beier, M. Rudy, K. Eren, J. I. Cervantes, B. Xu, F. Beuttenmueller, A. Wolny, C. Zhang, U. Koethe, F. A. Hamprecht and A. Kreshuk, *Nat. Methods*, 2019, **16**, 1226–1232.

14 O. Stamati, E. Andò, E. Roubin, R. Cailletaud, M. Wiebicke, G. Pinzon, C. Couture, R. C. Hurley, R. Caulk, D. Caillerie, T. Matsushima, P. Bésuelle, F. Bertoni, T. Arnaud, A. O. Laborin, R. Rorato, Y. Sun, A. Tengattini, O. Okubadejo, J.-B. Colliat, M. Saadatfar, F. E. Garcia, C. Papazoglou, I. Vego, S. Brisard, J. Dijkstra and G. Birmpilis, *J. Open Source Softw.*, 2020, **5**, 2286.